PCCP

ROYAL SOCIETY OF CHEMISTRY

PAPER

View Article Online
View Journal | View Issue



Cite this: *Phys. Chem. Chem. Phys.*, 2024, **26**, 15776

# Temperature-dependent NIR-CPL spectra of chiral Yb(III) complexes†

Annika Sickinger, ‡[a] Maxime Grasser, ‡[b] Bruno Baguenard,[c] Amina Bensalah-Ledoux,[c] Laure Guy,[a] Anh Thy Bui,[ad] Yannick Guyot,[c] Vincent Dorcet,[b] Fabrice Pointillart,[b] Olivier Cador,[b] Stéphan Guy,[c] Olivier Maury,[a] Boris Le Guennic[b] and François Riobé *[ae]

Received 28th March 2024,
Accepted 13th May 2024

DOI: 10.1039/d4cp01286k

rsc.li/pccp

Chiral, enantiopure Yb(III) complexes exhibit circularly polarized luminescence (CPL) in the near infrared (NIR) wavelength region. This CPL is quantified by the dissymmetry factor ($g_{lum}$). The excited state $^2F_{5/2}$ consists of six $m_{J'}$ states degenerated in three Stark levels, due to the crystal-field splitting (CFS), which are populated in accordance with the Boltzmann distribution. Consequently, room temperature CPL spectra are the sum of various - either positive or negative – contributions, that are practically impossible to quantify. To address this issue, an advanced setup enabling CPL measurements over a broad temperature range (300 to 4 K) has been developed. The interrelation of CFS, $g_{lum}$ and temperature was explored using a pair of enantiopure Yb(III) complexes, highlighting the individual contribution of each crystal-field sublevel to the overall CPL spectrum, as anticipated by simulations performed in the framework of multireference wave-functions. Hence, the CPL spectra of chiral lanthanide complexes were found to be indeed strongly temperature-dependent, as is the $g_{lum}$ dissymmetry factor, as a consequence of the variation in thermal sublevel population.



## Introduction

Circularly polarized luminescence (CPL), defined as an emission of light with a preferential helicity, has spurred renewed interest in chiral molecules and their fundamental studies.[1,2] Gradually evolving from mere laboratory curiosities, materials capable of emitting CPL are envisioned for diverse applications in fields such as bioimaging, chiral optoelectronic devices, and spintronics.[3–6] The intensity of this effect is described by the dissymmetry factor $g_{lum}$, calculated as the ratio of the left- and right-CPL intensity difference to the overall emitted intensity, scaling the theoretical maximum values to $\pm$ 2.[7] Besides a myriad of organic systems,[8] luminescent coordination complexes of transition metals featuring chiral properties are well-established as CPL emitters, but their characteristic $g_{lum}$ values remain rather low ($g_{lum} < 10^{-3}$).[3,9]

Since high luminescence dissymmetry factors are generally favored in transitions that are electric-dipole (ED) forbidden but magnetic-dipole (MD) allowed ($\Delta J = 0, \pm1$ (except $0 \leftrightarrow 0$)), trivalent complexes of f-block elements have emerged as particularly efficient emitters.[7,8,10,11] In this context, the record dissymmetry factor to date is $g_{lum}$ = 1.38 at 595 nm, matching the MD-allowed $^5D_0 \rightarrow {}^7F_1$ transitions, in a tetra-camphorate europium(III) complex, Cs[Eu[(+)-(hfbc)$_4$]] (hfbc = 3-heptafluorobutyryl camphorate) at 295 K.[12] This particularly favorable situation can also occur for certain transitions in other lanthanide ions, such as Sm(III), Tb(III), Dy(III) and Yb(III).[3,13–15] It is worth emphasizing that the dissymmetry factor in lanthanide complexes is not a characteristic of the molecule, but of each given f–f transition, and therefore will change depending on the emission wavelength.

This picture is further complicated by the lifting of the degeneracy of f-element spectroscopic levels ($^{2S+1}\Gamma_J$) by the crystal field, giving rise to a set of Stark sublevels. This splitting of degenerate levels, known as crystal-field splitting (CFS), is related to the symmetry of the complex and plays a crucial role in the interpretation of molecular magnetic and luminescence properties.[16–19] Furthermore, CFS has a substantial yet largely overlooked impact on CPL. While Eu(III) is the simplest case due to its non-degenerate $^5D_0$ emissive state, in all other Ln(III)

[a] *Univ. Lyon, ENS de Lyon, CNRS, Laboratoire de Chimie UMR 5182, F-69342 Lyon, France. E-mail: francois.riobe@icmcb.cnrs.fr*
[b] *Univ Rennes, CNRS, ISCR (Institut des Sciences Chimiques de Rennes) UMR 6226, F-35000 Rennes, France*
[c] *Univ. Lyon, CNRS, Institut Lumière Matière UMR 5306, F-69622 Villeurbanne, France*
[d] *Univ. Bordeaux, CNRS, Bordeaux INP, ISM, UMR 5255, F-33400 Talence, France*
[e] *Univ. Bordeaux, CNRS, Bordeaux INP, ICMCB UMR 5026, F-33600 Pessac, France*

† Electronic supplementary information (ESI) available. CCDC 2245303 and 2245302. For ESI and crystallographic data in CIF or other electronic format see DOI: https://doi.org/10.1039/d4cp01286k

‡ These authors contributed equally.

ions, the emissive state displays a distinct CFS. Hence, assuming thermalization during the lifetime of long-lived excited states, each excited crystal field sublevel is populated as a function of temperature according to the Boltzmann distribution.[16,19] As a consequence, most room temperature CPL spectra that have been reported so far are the sum of all excited sublevels contributions that can be either positive or negative, and may not reflect the $g_{lum}$ of each isolated transition. In this context, we have recently emphasized the experimental bandwidth influences CPL measurements of lanthanide complexes and further exposes the variability of $g_{lum}$ values.[20] Focusing herein on the effects of variations in sublevel distributions, we remark that not only do they alter the CPL spectra, but also these temperature-dependent changes do not necessarily parallel the variations measured in luminescence. Thus, due to these separately evolving components, the $g_{lum}$ dissymmetry factor should be treated as a function of temperature ($g_{lum}(\lambda, T)$), at fixed instrumental conditions.

The present article proposes to address the abovementioned interrelation of CFS, $g_{lum}$ factor and temperature. To that end, a chiral Yb(III) complex was selected as this lanthanide conveniently presents radiative transitions between only two J-manifolds ($^2F_{5/2} \rightarrow {}^2F_{7/2}$) with predictable CFS, *i.e.*, 3 and 4 sublevels for the excited and ground states, respectively. Solid solutions of both enantiopure Yb(III) complexes (Scheme 1) dispersed in a polymer matrix were used to measure variable-temperature CPL on a novel spectroscopy set-up, pioneering measurements at cryogenic temperatures. CPL measurements unprecedentedly spanning from room temperature (RT) down to the lower limit of the cryogenic range at 4 K were subjected to multireference wave-function-based calculations. These analyses revealed the intricate interplay of underlying spectral contributions, as well as the current limits of CPL interpretations with presently available state-of-the-art methods.

## Results and discussion

The chiral helicoidal Yb(III) complex, derived from the structure reported in 2007 by the group of Gunnlaugsson,[21] is formed by the wrapping of three chiral *R,R* (or *S,S*) pyridyldiamide ligands around the central ion and stabilized by inter-ligand π–π interactions. In order to improve its extinction coefficient, luminescence, and CPL brightness, we further decorated the dipicolinic acid-derived ligand structure with a π-conjugated dialkylaminophenylethynyl antenna. The resulting compounds [Yb(*S,S*-$L^{NHex2}$)$_3$(OTf)$_3$] and [Yb(*R,R*-$L^{NHex2}$)$_3$(OTf)$_3$] (Scheme 1) – respectively named **Δ-Yb** and **Λ-Yb** according to their helical chirality around the lanthanide ion – were obtained as orange microcrystalline powders (Fig. 1a) and fully characterized by $^1$H-NMR and FTIR spectroscopies as well as mass spectrometry (for synthetic details and complete characterization, see Scheme S1 and Fig. S3–S10, ESI†). $^1$H-NMR spectroscopy clearly indicated a single set of signals as expected for a complex with threefold symmetry, attesting its purity. We have previously demonstrated that in analogous Yb(III) complexes, the structure in solution, inferred from paramagnetic NMR, matched that obtained in crystal by X-ray diffraction.[17] In the present case, single crystals of **Δ-Yb** and **Λ-Yb** suitable for X-ray diffraction analysis of both enantiomers were obtained by layering di-*n*-butylether over a concentrated solution of the complex in methanol.

Contrary to previously reported derivatives obtained with related ligands,[17] the crystal structures were perfectly refined for both enantiomers. The two compounds crystallize in the orthorhombic $P2_12_12_1$ space group (Table S1, ESI†). The Yb(III) ion is in a $N_3O_6$ environment whose six oxygen and three nitrogen atoms belong to three $L^{NHex2}$ ligands (Fig. 1). The ligands' *S,S* and *R,R* absolute configurations induce Δ and Λ Yb(III)-centered chirality, respectively. Intramolecular π–π interactions are observed between each pyridyldiamide moiety and naphthyl groups of the other two ligands within the same complex (Fig. S11, ESI†). Although the hexyl chains prevent previously observed intermolecular π-stacking, the integrity of the crystal packing is supported by a templating effect of the triflate anion which connects two complexes through hydrogen

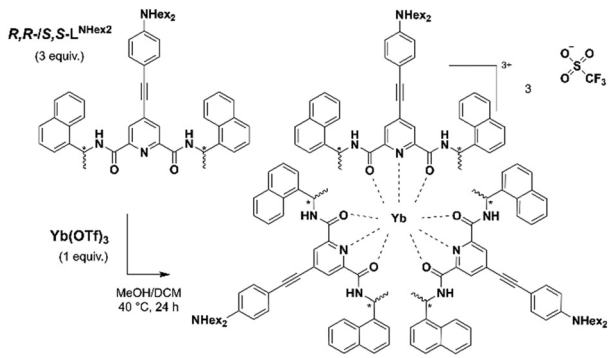


Scheme 1 Formation of the chiral ytterbium(III) complex.

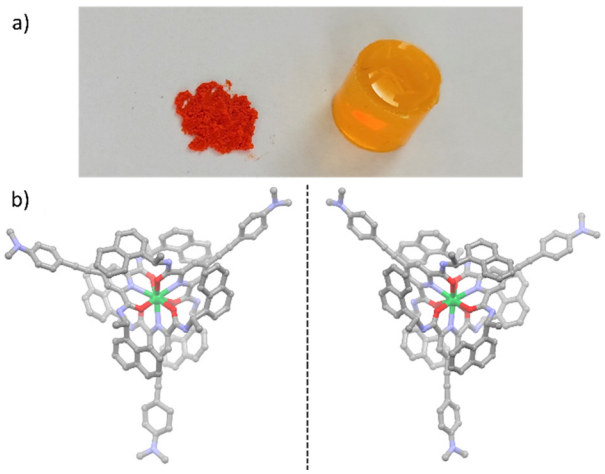


Fig. 1 (a) Pure powder of Yb(III) complex, on the left, and solution in PDMS polymer, on the right; (b) X-ray structures of [Yb(*S,S*-$L^{NHex2}$)$_3$(OTf)$_3$]/**Δ-Yb** (left) and [Yb(*R,R*-$L^{NHex2}$)$_3$(OTf)$_3$]/**Λ-Yb** (right). Hexyl chains are simplified; hydrogen atoms, solvent molecules and OTf-anions are omitted for clarity. Green, Yb; red, O; blue, N and grey, C.

binding interactions, *i.e.*, H···O and H···F short contacts (Fig. S12, ESI†).

We recently described a dual near-infrared CPL spectroscopy set-up that operates with parallel detections either in fast full-spectrum acquisition mode, thanks to a CCD camera and the combination of two inverted polarization encoded channels, or step-by-step wavelength scanning configuration using conventional analysis of polarization time modulation.[22] A closed-cycle helium cryostat was added to this set-up enabling variable temperature (VT) CPL monitoring in the 4–300 K range (Fig. S2, ESI†). While clearly advantageous in terms of structural control, microcrystalline samples were not used in chiroptical measurements to prevent all CPL artifacts that could arise from anisotropic media.[23] Likewise, albeit ubiquitous, organic glass solutions were dismissed to avoid adverse effects on the measurements caused by temperature-induced liquid to solid phase transition and anisotropies arising from possible cracks.[24] We instead opted for solid solutions of the complex immobilized in a polymer matrix. The solid sample was molded into a copper sample holder to ensure optimal thermal conduction (Fig. S13, ESI†). Importantly, the bottom of the holder cavity was removed to suppress reversed polarization generated by light reflection of the metallic surface.[25] Among the range of polymers suited for optical applications, poly(dimethylsiloxane) (PDMS) was preferred due to advantageous properties in terms of transparency, stability and processability.[26,27] In addition, the complexes are known to display poor stability and solubility in other classic polymers such as PMMA. The PDMS samples were prepared by mixing the pre-polymer of a two-part polymerization kit (Sylgard 184, Dow) with a concentrated solution of the complex in tetrahydrofuran (see ESI† for details). A significant improvement with regard to the previously described preparation[17] was achieved in the solubility of the complexes in the strongly hydrophobic polymer matrix, on account of the extended hexyl chains at the end of the conjugated antenna. After evaporation of solvents, the cross-linking agent was added and the viscous mixture was cured in the desired container (either an EPR tube for luminescence spectroscopy or directly in the CPL sample holder), resulting in a transparent elastic material, that is free of air bubbles (Fig. S13, ESI†). Notably, no precipitation was noticed, yielding samples of good optical quality.

The photophysical and chiroptical characterizations of the complexes were then performed either in methanol solution or in solid state using pure polycrystalline powders or PDMS-diluted samples. The orange color of the complexes is due to a broad, intense and structureless absorption band centered at 454 nm ($\varepsilon$ = 83 000 L mol$^{-1}$ cm$^{-1}$, Table S2, ESI†) assigned to intra-ligand charge transfer (ILCT) transitions (Fig. S14, ESI†). In addition, in concentrated solutions the characteristic f–f absorption band of Yb(III) was observed in the NIR (Fig. S15, ESI†). In order to exclude the occurrence of ligand dissociation upon dilution, absorption spectra were recorded in methanol solution of varying concentration (Fig. S16, ESI†). Even in very diluted solutions, complexes can be identified as the only absorbing species without any apparent free ligand-based absorption. For all samples, ILCT excitation (Fig. S17, ESI†) induced the characteristic emission profiles of Yb(III) in the NIR region, corresponding to the $^2F_{5/2} \rightarrow {}^2F_{7/2}$ transitions (Fig. 2a and Fig. S18 and 19, ESI†).[28] In addition, the luminescence

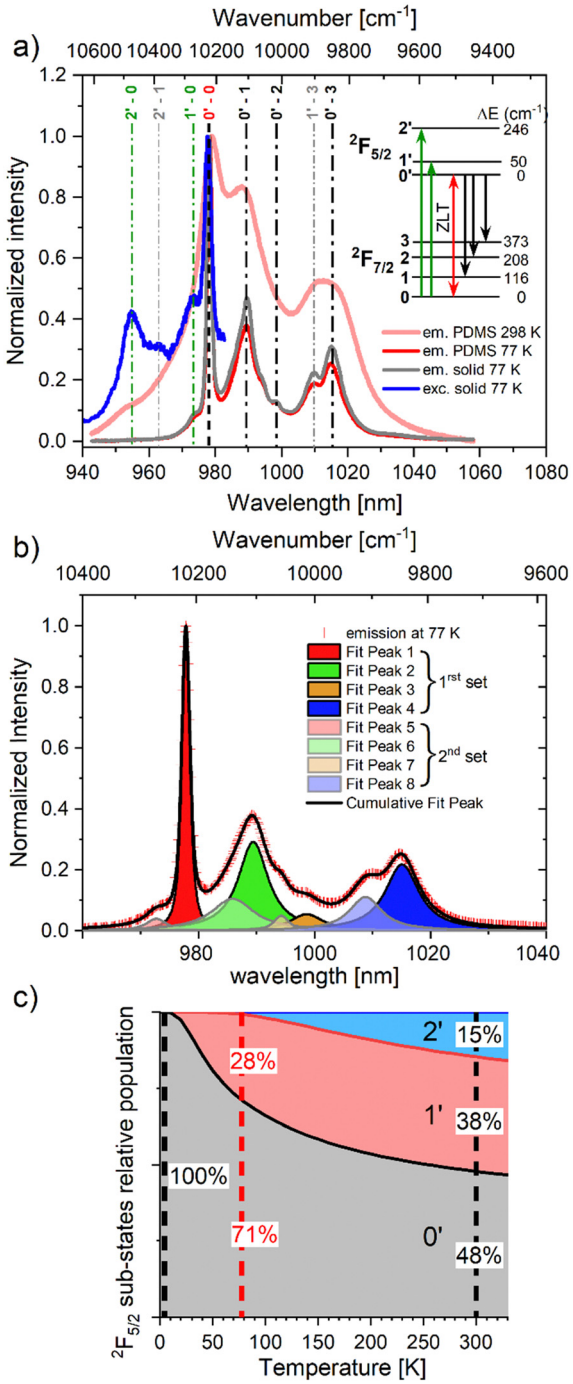


Fig. 2 (a) Normalized luminescence spectra of **Λ-Yb** in powders (grey line) and in PDMS (pink line: at RT, red line: at 77 K, $\lambda_{ex}$ = 350 nm). Corresponding excitation spectrum in the solid state at 77 K (blue line, $\lambda_{em}$ = 1020 nm). Inset: energy diagram for the CFS; (b) decomposition of the luminescence spectrum of **Λ-Yb** in PDMS matrix at 77 K using Voigt profiles (spectral bandwidth: 1 nm); (c) area chart of relative populations of the crystal-field excited state $^2F_{5/2}$ with respect to temperature.

lifetimes of the two enantiomers were measured in pure solids as well as in methanol and PDMS solution by monitoring the luminescence decay at 980 nm (Fig. S20, ESI†). Subsequent fitting with a mono-exponential model yielded values of $\tau$ = 4.8–5.9 μs (Table S3, ESI†) depending on the medium and in accordance with lifetimes found previously for Yb(III) complexes, corroborating the presence of a single emissive species in all examined conditions.[17,29,30] Decreasing the temperature down to 77 K resulted in a narrowing of the emission bands and a reduced contribution of hot bands (*i.e.* additional transitions from thermally populated $^2F_{5/2}$ Stark sublevels). As expected, identical emission features were obtained for both enantiomers. Remarkably, the emission was identical for the complexes in solution, in powders and in the polymer matrix, indicating that the structure of the complexes is preserved.

The excitation and emission spectra at 77 K corresponding to the $^2F_{5/2} \leftrightarrow {}^2F_{7/2}$ transitions allowed to establish an energy diagram that depicts the splitting of both energy levels (Fig. 2a). The two spectra exhibited a shared zero-phonon line ($0' \leftrightarrow 0$) at 978 nm, corresponding to a 10 224 ± 10 $cm^{-1}$ energy difference between the ground and excited states. Two additional contributions at 955 and 973 nm were observed in the excitation spectrum. These can confidently be assigned to the threefold CFS degeneracy of the $^2F_{5/2}$ excited state ($0'$, $1'$ and $2'$), providing its CFS energy diagram (0, 50, 246 ± 10 $cm^{-1}$).

We then set out to analyze the 77 K emission spectrum, which could be decomposed using Voigt functions[19] into at least 8 main contributions (Fig. 2b, Fig. S21, ESI†). The bands observed at 978, 990, 999 and 1015 nm (10 222, 10 106, 10 014 and 9849 ± 10 $cm^{-1}$) were assigned to the transitions from the lower $^2F_{5/2}$ excited sublevel to the four sublevels of the $^2F_{7/2}$ ground state (0–3, Fig. 2a). This assignment was supported by the 4 individual bands decomposition obtained with the 4 K emission spectrum (Fig. S22, ESI†). The four remaining transitions formed a second set of contributions with lower intensities that is shifted to higher energy by approximately 50 $cm^{-1}$ and therefore can be assigned to emission from the $1'$ excited state ($1' \rightarrow$ 0–3). Although we must mention the presence of minor additional features, likely attributed to vibronic contributions (for instance, at 9750–9600 $cm^{-1}$), the overall emission spectrum at 77 K is adequately described by the CFS energy diagram proposed for the $^2F_{7/2}$ ground state: 0, 116, 208, 373 ± 10 $cm^{-1}$ (inset in Fig. 2a). It is worth noting that the CFS energy of the ground state multiplet, $\Delta_{CFS}$ = 373 $cm^{-1}$, is also consistent with other threefold-symmetric Yb(III) complexes.[17,29,31] From the energy splitting of the $^2F_{5/2}$ state, we calculated the anticipated variation of relative population with respect to temperature (Fig. 2c).[17]

Chiroptical characterizations of the complexes were carried out using a combination of various techniques. Visible electronic circular dichroism (ECD) (Fig. S23, ESI†) shows the Cotton effect in all ligand-centered transitions including the low energy ILCT one. In addition, both ECD and CPL in the NIR region were investigated in concentrated solutions at room temperature, using our aforementioned set-up (Fig. 3).[21] As already observed, since they can have positive and negative values, the sub-contributions of each chiroptical spectrum

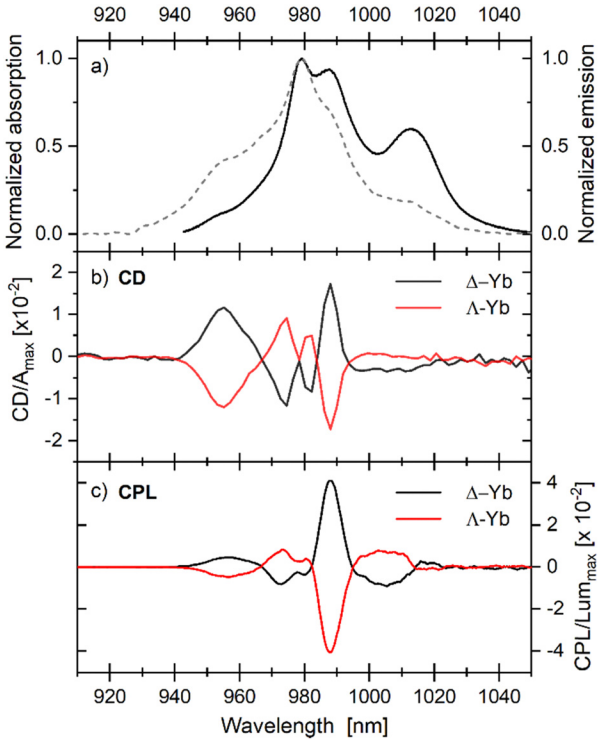


Fig. 3 Near-infrared chiroptical characterizations at room temperature in methanol solution of **Δ-Yb** (black lines) and **Λ-Yb** (red lines). (a) Normalized absorption (dash line) and emission (solid line, $\lambda_{ex}$ = 350 nm), (b) CD spectra ($C$ = 0.86 mM) and (c) CPL spectra ($C$ = 0.35 mM, $\lambda_{ex}$ = 365 nm).

(ECD and CPL) are more discernible than in their non-polarized counterparts.[17] The profile of ECD and CPL of the $^2F_{5/2} \leftrightarrow {}^2F_{7/2}$ transitions are similar because all sublevels are thermally populated at room temperature and thus the same dissymmetry factors are involved in both spectra. In both cases, the most intense band is centered at 988 nm with strong dissymmetry factors in absorption ($g_{abs}$ = 0.025) and in emission ($g_{lum}$ = 0.088).

Finally, the CPL spectra of the doped PDMS samples were recorded using the above-described VT-CPL set-up. The low-temperature measurements were performed by cooling down the sample to 150, 80, 30 and 4 K. At each temperature, the CPL spectra of the two enantiomers remain mirror images of each other. More interestingly, the CPL profile is strongly modified as a function of temperature (Fig. 4). In particular, the CPL signals observed at higher energy than the zero line (from 920 to 975 nm), corresponding to 'hot bands' emission ($2' \rightarrow 0$ at 955 nm and $1' \rightarrow 0$ at 973 nm, Fig. 4b inset) vanish upon cooling due to progressive depopulation of upper excited sublevels of the $^2F_{5/2}$ emissive level. The global shape of the CPL spectrum presents less features at lower temperature in the absence of the $2'$ and $1'$ contributions of the $^2F_{5/2}$. Finally, at 4 K, the CPL spectrum originates exclusively from the fundamental 0' sublevels (Fig. 4) and can be decomposed into the 4 expected contributions for both enantiomers (Fig. S24, ESI†).

To give more insight into these chiroptical properties, the CPL spectrum of **Λ-Yb** was calculated with a multireference wavefunction-based methodology (SA-RAS[13,0,2,0,7,5]CI-PT2/RASSI-SO

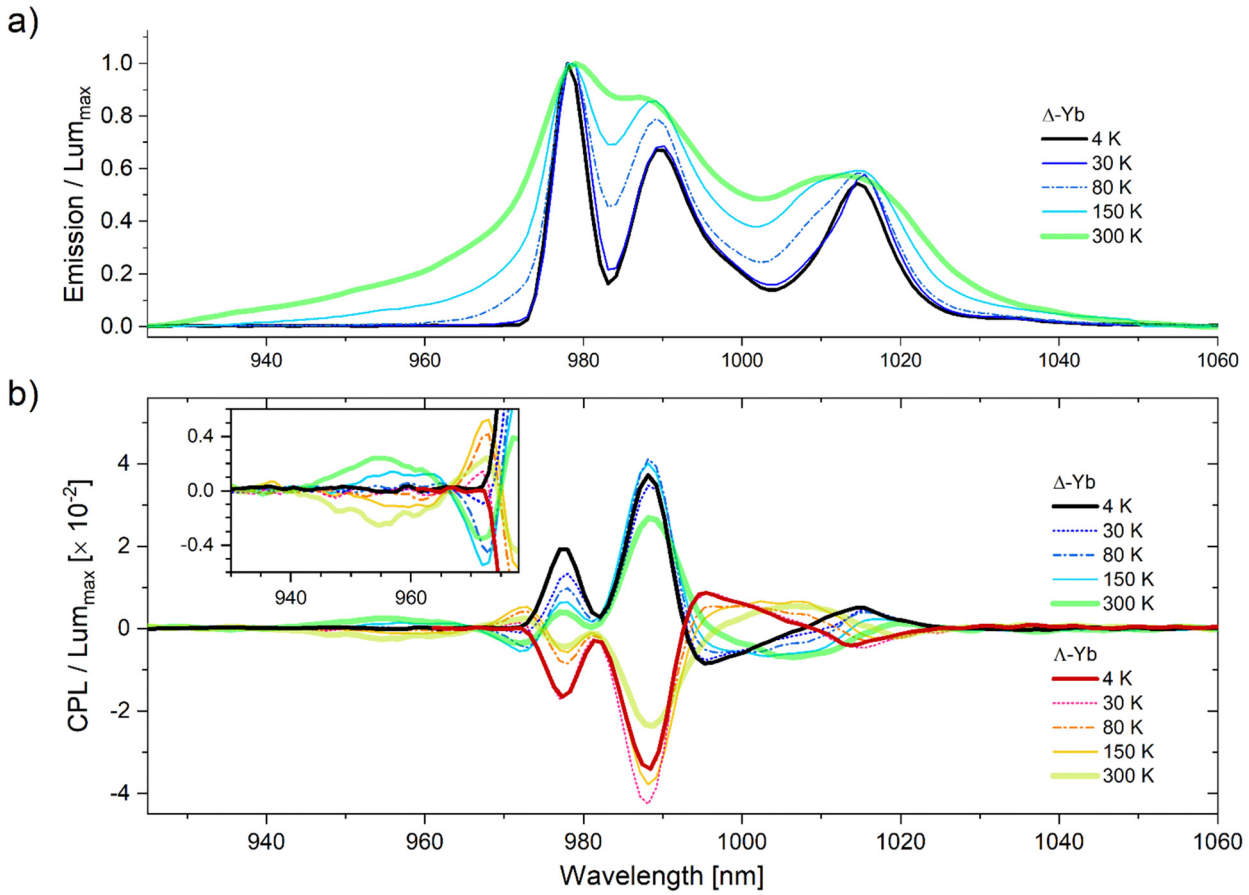


Fig. 4 VT spectra of the two $Yb^{3+}$ complexes, in PDMS at 4, 30, 80, 150 and 300 K ($\lambda_{ex}$ = 365 nm). (a) VT-luminescence spectra for **Δ-Yb**; (b) VT-CPL spectra. Inset shows enlarged region of hot bands. For each temperature, both emission and CPL spectra have been normalized by dividing them by the highest emission intensity (displayed in (a) and Fig. S24, ESI†) at 978.

level of theory) recently developed and already successfully applied to various europium, samarium and ytterbium complexes.[32–35] Calculations were carried out on the model complex shown in Fig. S27 (see Computational Details in ESI†).[17] The simulated CPL at RT (room temperature, Fig. S28, ESI†) reproduces the experimental observations well and highlights through Boltzmann population analysis the contribution of 'hot bands' in the RT-CPL signal. The key calculated quantities are presented in Table S6 (ESI†), allowing to analyze each CPL transition through the electric dipole, magnetic dipole and electric quadrupole transition moments involved. In particular, one can note that oscillator strengths of the electric quadrupole transition moments are lower than the ED and MD transition moments by four to seven orders of magnitude, indicating that they do not play a key role in the transitions. Simulated CPL spectra allow to unravel which transitions contribute to each observed CPL band (Fig. S28, ESI†). We first note that the calculated $2' \rightarrow 0$, $1' \rightarrow 0$, $1' \rightarrow 3$ and $0' \rightarrow 3$ are well positioned and their evolution in temperature well reproduced the experimental observed trend. Moreover, not only does the main negative CPL band of **Λ-Yb** at 985 nm at RT correspond to the $0' \rightarrow 1$ transition, but it also contains non-negligible contributions from the $1' \rightarrow 2$ and $2' \rightarrow 3$ transitions. Taking the analysis further, the computed $0' \rightarrow 2$ transition tends to be overcome by the transition from the $1'$ sublevel whose contribution intensifies with the temperature ($\geq$14% for $T \geq 80$ K; Table S5, ESI†). This behavior is in accordance with the experimental data. The main difference between theory and experiment concerns the band calculated at 978 nm (attributed to both $0' \rightarrow 0$ and $1' \rightarrow 1$) whose sign is reversed w.r.t experiment. However, the decrease in intensity accompanying temperature increase is consistent with experimental findings. This discrepancy may have several computational origins that the currently developed methodology cannot fully address. In particular, while the electronic structure is calculated at the state-of-the art, the static approach that only consider single geometry and precludes vibronic effects and fluxional evolutions may find its limitation even for describing behaviors at low temperature.

In order to appreciate the observed variations in CPL and luminescence with respect to temperature, the dissymmetry factors ($g_{lum}$) were determined across the entire emission range at the different temperature steps $T_i$ (Fig. 5):

$$g_{lum}(\lambda, T_i) = \frac{2I_{CPL}(\lambda, T_i)}{I_{em}(\lambda, T_i)}$$

 

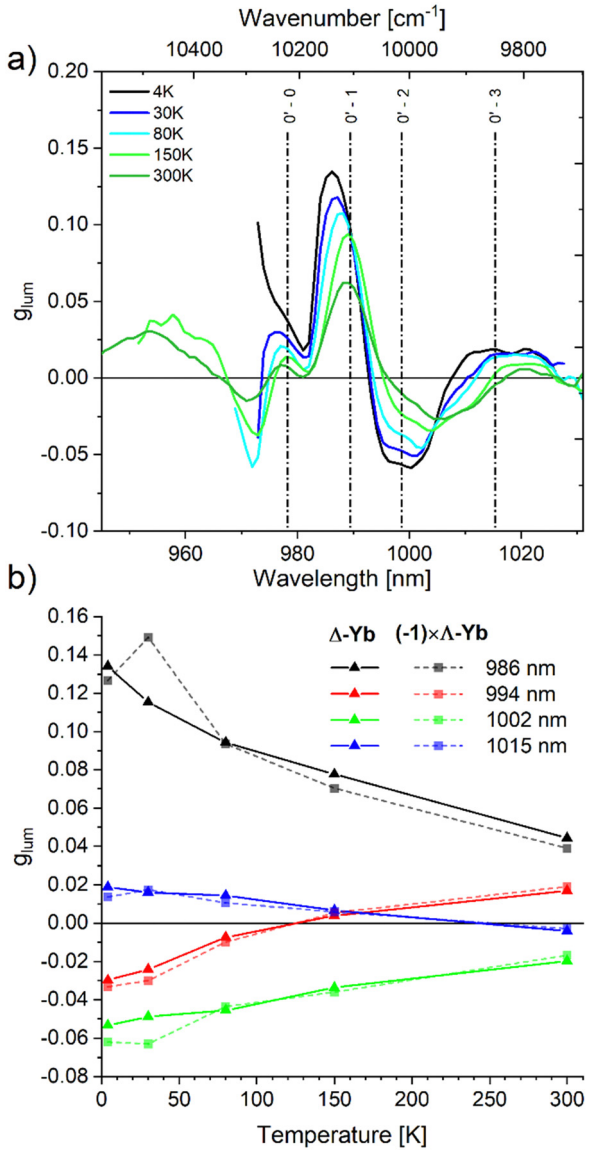


Fig. 5 (a) Variations of the emission dissymmetry factor, $g_{lum}$, of **Δ-Yb** over its emission range at different temperatures (cut-off at 5% of the emission maximum for each temperature to discard erratic values at low intensities) with previously determined transitions energies from the 0′ excited sublevel (Fig. 2a) (b) variation of dissymmetry factors with temperature at selected wavelengths (opposite-sign $g_{lum}$ values are plotted for **Λ-Yb**).

Ideally, in the absence of structural modifications, at a given temperature the $g_{lum}$ factor should behave as a constant for each transition, producing a plateau value over the corresponding emission band. However, even at 4 K, we observed a different behavior. Firstly, the $g_{lum}$ plots revealed a continuously varying function of wavelength, instead of 4 discrete values (Fig. 5a). Furthermore, the $g_{lum}$ maxima appear at wavelengths that do not coincide with any of the identified transitions (Fig. 5a) or with the local maxima observed in luminescence and CPL spectra (Fig. 3 and 4). These discrepancies are due to spectral overlap between contributions of different signs that results in a wavelength-dependent $g_{lum}$, which is the sum of all contributions weighted by their respective intensities.[20] To estimate the true $g_{lum}$ associated with each $0' \rightarrow$ 0–3 transition, the areas of individual components from the Gaussian decompositions of CPL (Fig. S24, ESI†) were compared with their luminescence counterparts (Fig. S22, ESI†) at 4 K (Fig. S26, ESI†). The −0.011 and 0.016 values extracted for the $0' \rightarrow 3$ transition at 1015 nm, for **Λ-Yb** and **Δ-Yb** respectively, matched the $g_{lum}$ plateaus observed, as this transition is spectrally well isolated. In contrast, in other regions, the continuous plot underestimates $g_{lum}$ for $0' \rightarrow 1,2$ and presents uncertain values around the $0' \rightarrow 0$ transition.

Bearing in mind the nontrivial effect of this spectral overlap,[20] the variation of $g_{lum}$ with temperature can now be discussed. Increasing temperature leads firstly to a broadening of each spectral line (Fig. 4) and thus to an enhancement of band overlaps. Secondly, as previously mentioned, thermally populated 1′ and 2′ sublevels of $^2F_{5/2}$ cause the appearance of additional bands at lower wavelengths in both emission and CPL spectra (Fig. 4). As seen in the $g_{lum}$ plot, these ''hot bands'' display dissymmetry factors with comparable magnitudes to those observed at low temperature (Fig. 5), however their signs can differ from their counterparts originating from the 0' sublevel. Combined with thermal broadening, the increase in relative intensities of these contributions profoundly alter the overall shape of the $g_{lum}$ curve. The peak positions and their intensities change with temperature. Consequently, the selection of any specific wavelength like the wavelength at maximal luminescence or $|g_{lum}|$ to monitor CPL variation with temperature appears arbitrary.

It is well illustrated by comparing the evolution of $g_{lum}$ with respect to temperature at four fixed wavelengths ($\lambda$ = 986, 994, 1002, 1015 nm) for both enantiomers (Fig. 5b and Table S4, ESI†), plotting the values measured with **Λ-Yb** with the opposite sign to facilitate comparisons. The same tendencies were observed for both compounds, confirming the conservation of the mirror image nature of the CPL spectra. On the other hand, significant variations were found at all wavelengths. For example, the most intense dissymmetry observed for **Δ-Yb** at 986 nm declined more than threefold, from 0.13 at 4 K to 0.04 at 300 K. Strikingly, Fig. 5b also evidences that even the sign of the $g_{lum}$ factor can change at some specific wavelengths.

## Conclusions

For the first time, this study demonstrates experimentally, through the use of a VT-CPL setup, that the CPL spectra of chiral lanthanide complexes are dramatically affected by temperature. This is due both to the thermal broadening of emission lines, that exacerbates the spectral merging of the different transitions, and to the Boltzmann's equilibration of the different crystal-field sublevels in the excited state. This experiment also highlights that transitions dissymmetry factors ($g_{lum}$) are seldom directly measured by CPL spectrometry, even at low temperature due to the overlay between emission lines. In this regard, we hope

that this study will raise concern about the somewhat vague nature of the $g_{lum}$ value as a characteristic of a given chiral lanthanide(III) compound. For lanthanide ions, not only does this value depend on the wavelength but it can also vary with temperature, even in the case of non-degenerated excited levels due to inherent thermal broadening of emission lines (*e.g.*, Eu(III)). It is thus crucial that precise experimental parameters be stated in any CPL measurement (temperature, spectrometer bandwidth) for proper comparisons to be meaningful.

We provide all raw data associated with this study in ESI† to facilitate their use by the community. We believe cryogenic-temperature measurements hold the key to lanthanide CPL characterization and their fundamental understanding. Current limitations arising from the inherent broadening of emission lines observed in the selected structure hinder a complete interpretation of the measured CPL spectra.

## Author contributions

BLG, OM and FR designed and supervised the study. AS and ATB synthetized the complexes. FP, VD and OC solved the XRD structures. AS, OM and FR performed the non-polarized spectroscopy. YG measured the NIR emission decays. AS and LG prepared the PDMS samples. AS, BB, AB-L and SG performed all the chiroptical measurements. MG and BLG carried out the multireference wavefunction simulations. All the authors discussed and contributed to the manuscript preparation. All authors have given approval to the final version of the manuscript.

## Conflicts of interest

There are no conflicts to declare.

## Acknowledgements

We thank the French National Research Agency (ANR) through the project SMMCPL (ANR-19-CE29-0012). M. G. and B. L. G. thank the French GENCI/IDRIS–CINES center for high–performance computing resources.

## References

1 J. P. Riehl and F. S. Richardson, *Chem. Rev.*, 1986, **86**, 1–16.
2 J. R. Brandt, F. Salerno and M. J. Fuchter, *Nat. Rev. Chem.*, 2017, **1**, 1–12.
3 L. Arrico, L. Di Bari and F. Zinna, *Chem. – Eur. J.*, 2021, **27**, 2920–2934.
4 G. Longhi, E. Castiglioni, J. Koshoubu, G. Mazzeo and S. Abbate, *Chirality*, 2016, **28**, 696–707.
5 J. R. Brandt, X. Wang, Y. Yang, A. J. Campbell and M. J. Fuchter, *J. Am. Chem. Soc.*, 2016, **138**, 9743–9746.
6 J. Han, S. Guo, H. Lu, S. Liu, Q. Zhao and W. Huang, *Adv. Opt. Mater.*, 2018, **6**, 1800538.
7 B. Doistau, J.-R. Jiménez and C. Piguet, *Front. Chem.*, 2020, **8**, 1–27.
8 J. Kumar, T. Nakashima and T. Kawai, *J. Phys. Chem. Lett.*, 2015, **6**, 3445–3452.
9 H.-Y. Wong, W.-S. Lo, K.-H. Yim and G.-L. Law, *Chem*, 2019, **5**, 3058–3095.
10 R. Carr, N. H. Evans and D. Parker, *Chem. Soc. Rev.*, 2012, **41**, 7673–7686.
11 K. Staszak, K. Wieszczycka, V. Marturano and B. Tylkowski, *Coord. Chem. Rev.*, 2019, **397**, 76–90.
12 J. L. Lunkley, D. Shirotani, K. Yamanari, S. Kaizaki and G. Muller, *J. Am. Chem. Soc.*, 2008, **130**, 13814–13815.
13 O. G. Willis, F. Zinna and L. Di Bari, *Angew. Chem., Int. Ed.*, 2023, **62**, e202302358.
14 B.-A. N. Willis, D. Schnable, N. D. Schley and G. Ung, *J. Am. Chem. Soc.*, 2022, **144**, 22421–22425.
15 J. A. Adewuyi, N. D. Schley and G. Ung, *Chem. – Eur. J.*, 2023, **29**, e202300800.
16 D. Guettas, F. Gendron, G. Fernandez Garcia, F. Riobé, T. Roisnel, O. Maury, G. Pilet, O. Cador and B. Le Guennic, *Chem. – Eur. J.*, 2020, **26**, 4389–4395.
17 F. Gendron, S. D. Pietro, L. Abad Galán, F. Riobé, V. Placide, L. Guy, F. Zinna, L. D. Bari, A. Bensalah-Ledoux, Y. Guyot, G. Pilet, F. Pointillart, B. Baguenard, S. Guy, O. Cador, O. Maury and B. Le Guennic, *Inorg. Chem. Front.*, 2021, **8**, 914–926.
18 P. R. Nawrocki and T. Just Sørensen, *Phys. Chem. Chem. Phys.*, 2023, **25**, 19300–19336.
19 V. R. M. Nielsen, P. R. Nawrocki and T. J. Sørensen, *J. Phys. Chem. A*, 2023, **127**, 3577–3590.
20 A. Sickinger, B. Baguenard, A. Bensalah-Ledoux, Y. Guyot, L. Guy, F. Pointillart, O. Cador, M. Grasser, B. Le Guennic, F. Riobé, O. Maury and S. Guy, *J. Mater. Chem. C*, 2024, **12**, 4253–4260.
21 J. P. Leonard, P. Jensen, T. McCabe, J. E. O'Brien, R. D. Peacock, P. E. Kruger and T. Gunnlaugsson, *J. Am. Chem. Soc.*, 2007, **129**, 10986–10987.
22 B. Baguenard, A. Bensalah-Ledoux, L. Guy, F. Riobé, O. Maury and S. Guy, *Nat. Commun.*, 2023, **14**, 1065.
23 J. H. Freudenthal, E. Hollis and B. Kahr, *Chirality*, 2009, **21**, E20–E27.
24 M. Montalti, A. Credi, L. Prodi and M. T. Gandolfi, *Handbook of Photochemistry*, CRC Press, 2006.
25 F. Zinna, M. Pasini, F. Galeotti, C. Botta, L. Di Bari and U. Giovanella, *Adv. Funct. Mater.*, 2017, **27**, 1603719.
26 A. S. Cruz-Félix, A. Santiago-Alvarado, J. Márquez-García and J. González-García, *Heliyon*, 2019, **5**, e03064.
27 S. Seethapathy and T. Górecki, *Anal. Chim. Acta*, 2012, **750**, 48–62.
28 J.-C. G. Bünzli and C. Piguet, *Chem. Soc. Rev.*, 2005, **34**, 1048.
29 X. Yi, K. Bernot, V. Le Corre, G. Calvez, F. Pointillart, O. Cador, B. Le Guennic, J. Jung, O. Maury, V. Placide, Y. Guyot, T. Roisnel, C. Daiguebonne and O. Guillou, *Chem. – Eur. J.*, 2014, **20**, 1569–1576.
30 A. T. Bui, M. Beyler, A. Grichine, A. Duperray, J.-C. Mulatier, Y. Guyot, C. Andraud, R. Tripier, S. Brasselet and O. Maury, *Chem. Commun.*, 2017, **53**, 6005–6008.

31 C. Reinhard and H. U. Güdel, *Inorg. Chem.*, 2002, **41**, 1048–1055.
32 F. Gendron, B. MooreII, O. Cador, F. Pointillart, J. Autschbach and B. Le Guennic, *J. Chem. Theory Comput.*, 2019, **15**, 4140–4155.
33 F. Gendron, M. Grasser and B. Le Guennic, *Phys. Chem. Chem. Phys.*, 2022, **24**, 5404–5410.
34 K. Dhbaibi, M. Grasser, H. Douib, V. Dorcet, O. Cador, N. Vanthuyne, F. Riobé, O. Maury, S. Guy, A. Bensalah-Ledoux, B. Baguenard, G. L. J. A. Rikken, C. Train, B. Le Guennic, M. Atzori, F. Pointillart and J. Crassous, *Angew. Chem., Int. Ed.*, 2023, **62**, e202215558.
35 M. Grasser and B. Le Guennic, *Phys. Chem. Chem. Phys.*, 2024, **26**, 7203–7210.